2D EPID dosimetry for an MR-linac: proof of concept

Torres-Xirau, I.; Olaciregui-Ruiz, I.; Heide, U.A. van der; Mans, A.

Two-dimensional EPID dosimetry for an MR-linac: Proof of concept

Iban Torres-Xirau[a)], Igor Olaciregui-Ruiz, Uulke A. van der Heide, and Anton Mans
Department of Radiation Oncology, The Netherlands Cancer Institute–Antoni van Leeuwenhoek Hospital, Amsterdam, The Netherlands

(Received 28 January 2019; revised 29 May 2019; accepted for publication 29 May 2019; published 9 July 2019)

Purpose: At our institute, *in vivo* patient dose distributions are reconstructed for all treatments delivered using conventional linacs from electronic portal imaging device (EPID) transit images acquired during treatment using a simple back-projection model. Currently, the clinical implementation of MRI-guided radiotherapy systems, which aims for online and real-time adaptation of the treatment plan, is progressing. In our department, the MR-linac (Unity, Elekta AB, Stockholm, Sweden) is now in clinical use. The aim of this work is to demonstrate the feasibility of two-dimensional (2D) EPID dosimetric verification for the magnetic resonance (MR)-linac by comparing back-projected EPID doses to ionization chamber (IC) array dose distributions.
Materials and methods: Our conventional back-projection algorithm was adapted for the MR-linac. The most important changes involve modeling of the attenuation by and scatter from the cryostat. The commissioning process involved the acquisition of square field EPID measurements using various phantom setups (varying SSD, phantom thickness, and field size). Commissioning models were created for gantry 0°, 90°, and 180° and verified by comparing EPID-reconstructed 2D dose distributions to measurements made with the OCTAVIUS 1500 IC array (PTW, Freiburg, Germany) for two prostate and one rectum IMRT plans (25 beams total). The average of the γ parameters (y-mean and y-pass rate) and the dose difference at a reference point were reported. Due to their construction, the attenuation of couch, bridge, and cryostat shows a much stronger dependence on gantry angle in the MR-linac compared to conventional linacs. We present a method to correct for these effects. This method is validated by dose reconstruction of the 25 intensity-modulated radiation therapy beams recorded at a certain gantry angle using the model of another gantry angle, combined with the correction method.
Results: For dose verification performed at a gantry angle identical to the commissioned model, the average y-mean and y-pass rate values (3% global dose, 2 mm, 10% isodose) were 0.37 $\pm$ 0.07 and 98.1, 95% CI [98.1 $\pm$ 2.4], respectively. The average dose difference at the reference point was $-0.5\% \pm 1.8\%$. Verification at gantry angles different from the commissioned model (i.e., using the gantry angle dependent correction) reported 0.39 $\pm$ 0.08 and 97.6, 95% CI [96.9, 98.3] average y-mean and y-pass rate values. The average dose difference at the reference point was $-0.1\% \pm 1.8\%$.
Conclusion: The EPID dosimetry back-projection model was successfully adapted for the MR-linac at gantry 0°, 90°, and 180°, accounting for the presence of the MRI housing between phantom (or patient) and the EPID. A method to account for the gantry angle dependence was also tested reporting similar results. [https://doi.org/10.1002/mp.13664]

Key words: dose verification, EPID, MR-linac, portal dosimetry, QA, unity

1. INTRODUCTION

Although electronic portal imaging devices (EPIDs) were originally designed for patient position verification, their use for dosimetric applications has been acknowledged both for pretreatment and *in vivo* dose verification. The dose response characteristics of amorphous silicon (a-Si) EPIDs have been broadly studied,[1–8] and several EPID-based solutions are being used both for intensity-modulated radiation therapy (IMRT)[9–15] and VMAT[16–20] treatments.

Recently, treatment machines combining a radiation source with an MRI system have been developed and are clinically used. In our department, the MR-linac (Unity, Elekta AB, Stockholm, Sweden)[21,22] has been installed and patient treatments have started. The system is equipped with an EPID mounted on the rotating gantry, opposite to the accelerator head, allowing for simultaneous beam irradiation, EPID acquisition, and MR imaging.[23]

Online adaptive strategies in MRIgRT will become clinically feasible[24] as the result of the ongoing developments in fast recontouring and replanning. In this context, independent tools for the verification of these adaptive treatments will become imperative. Existing pretreatment tools for quality assurance (QA) in the MR-linac are typically time-consuming solutions which, besides, are not applicable for an online adaptive workflow.[25–28] Alternative patient-specific QA solutions have been proposed, such as fast sanity checks on the adapted plan,[29] *in vivo* geometrical accuracy of the delivery using EPID images,[30] or the use of independent calculations fed with linac log files.[31–34]

An MR-only workflow would allow for MRI-based delineation while performing dose calculation on a synthetic computed tomography (CT) derived from that MRI study. The use of log files in combination with an independent dose calculation algorithm using the synthetic CT is an alternative treatment verification method. However, this approach relies on the correctness of the log files and synthetic CT, and independent dose algorithms that consider the magnetic field are not widely available.

Currently, in all institutions that have started treating patients on the MR-linac, the dosimetric verification of adapted plans if performed is done after the treatment fraction using a detector array or film in combination with a phantom. The use of transit EPID dosimetry provides a complementary solution to these methods, able to perform an independent end-to-end check of the entire chain, verifying data transfer, dose delivery, patient setup, MLC calibration, and dose calculation,[35] and also synthetic CT determination. Moreover, the EPID is already attached to the machine, and allows for automation and even in real-time treatment verification.[36,37] However, it also comes with limitations given the position of the panel with respect to the beam, and when used without taking the magnetic field into account in the back-projection dose engine.

We have shown the dosimetric characteristics of the EPID to be similar in the MR-linac compared to conventional linacs.[38] Furthermore, the magnetic field at the EPID location is very low (the time-varying component during imaging even lower) and has been demonstrated not to influence the EPID images.[38] This suggests feasibility of the adaptation of existing back-projection models to the MR-linac geometry. The feasibility of correcting EPID images for the presence of extra scattering and attenuating material between phantom and EPID has also been demonstrated.[39] The aim of this study is to bring all these prior results together, and demonstrate the feasibility of back-projection EPID dosimetry for the MR-linac by comparing 2D EPID-reconstructed dose distributions to absolute dose measurements in a phantom.

2. MATERIALS AND METHODS

2.A. Accelerator, EPID, acquisition software, and measuring equipment

The MR-linac system combines a 7-MV flattening filter free (FFF) beam linac (Elekta AB, Stockholm, Sweden) with an integrated wide bore 1.5 T MRI scanner (Philips Medical Systems, Best, the Netherlands). The MR-linac uses an Elekta Agility-based multi-leaf collimator (MLC) consisting of 160 leaves with a projected width of a single leaf of 0.72 cm at the isocenter plane.

The accelerator and EPID are mounted on a ring gantry built around the MRI scanner. The source-to-isocenter distance is 143.5 cm, and the source-to-detector distance (SDD) is fixed to 265.3 cm, resulting in a magnification factor of 1.84. The central region of the magnet is free of gradient coils and shimming hardware, allowing for minimal and homogenous attenuation of the beam by the cryostat. This region determines the maximum allowed field size in the longitudinal direction ($\pm$11 cm at isocenter). The effective size of the beam exiting the MRI scanner is larger due to divergence, limiting the EPID acquisition of unattenuated beams to an irradiation field of a maximum of $\pm$4.8 cm in each direction of the longitudinal axis at the isocenter. For larger fields, the exit beam's dimensions exceed the coil-free region, and therefore, the exit beam is inhomogeneously attenuated. Moreover, due to the noncentered position of the EPID with respect to the beam axis, fields exceeding 8 cm in the positive longitudinal axis are not entirely captured by the EPID. Figure 1 illustrates the EPID position in the MR-linac geometry and the characteristics of acquired images. Therefore, in this study, the reconstructed dose distributions are truncated at $\pm$5.6 cm, close to the border of the area of homogenous attenuation.

Due to the rigid ring gantry on the Unity system, the EPID sag is smaller than in conventional linacs. On our system, the isocenter position on the panel was determined to be stable within 0.5 mm, which we considered negligible to our purposes. The Elekta iViewGT panel is an a-Si flat panel X-ray detector (XRD 1642 AP, Perkin Elmer Optoelectronics, Wiesbaden, Germany) with a 41 $\times$ 41 cm^2 detection area (1024 $\times$ 1024 pixels), and a pixel pitch of 0.4 mm. Images were acquired using Elekta's MVIC software. Array measurements were performed using an MR-compatible OCTAVIUS 1500 2D detector array (PTW, Freiburg, Germany), having 1405 vented ICs with 7.1 mm center-to-center distance, with an uncertainty of $\pm$0.5%, which was cross-calibrated to a known value for a reference beam.

2.B. Back-projection algorithm for the MR linac

2.B.1. Rationale

The conventional back-projection algorithm requires the portal dose distribution at the EPID level, the transmission through the phantom (or patient), and the geometry of the phantom (or patient). For the determination of the portal dose distribution at the EPID level, the parameters of our algorithm are fitted against IC dose measurements performed at the level of the EPID. Such measurements are made by an IC inside a cylindrical miniphantom at the location of the EPID.[12,40] This is impossible in the MR-linac due to the location of the panel, as there is no physical space to execute such measurements. Therefore, similar measurements were made at the isocenter and rescaled to the EPID level using the inverse square law (ISQL), to be used as surrogate for measurements at position of the EPID in the absence of the cryostat. The purpose of these adaptations to the back-projection algorithm is to estimate the attenuation and scatter sensed by the EPID, generated by the cryostat, couch, and bridge. Using this result, the primary dose at the EPID level can be determined. Effectively, the adapted algorithm removes the influence of the cryostat and the intrinsic scatter generated within the EPID in the conversion from pixel values to portal dose distributions at EPID level. The other parts of the back-projection algorithm are not modified.

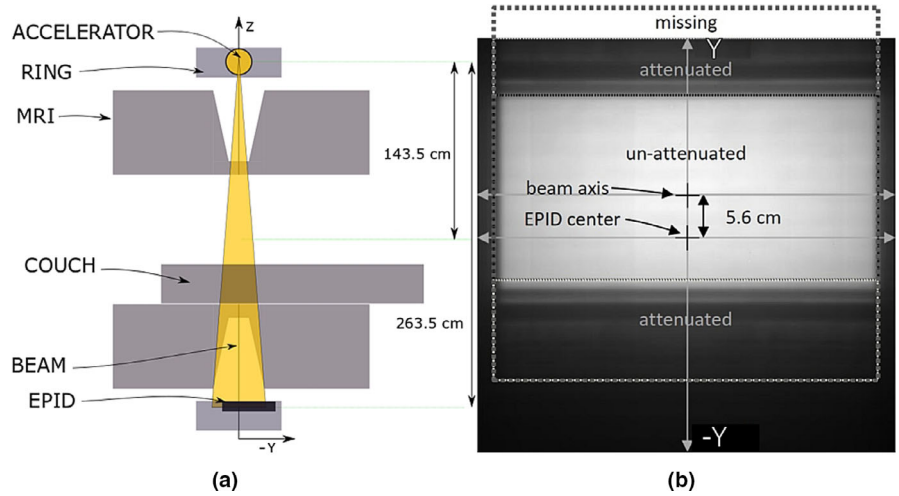

FIG. 1. (a) Magnetic resonance (MR)-linac cross section. In the Y direction, the beam center is not aligned with the center of the electronic portal imaging device (EPID). Therefore, parts of large fields fall outside the EPID detection area. (b) EPID image of a 20 × 20 cm^2 (FFF) beam. The centers of the EPID and the beam are marked with a cross, and a dashed line shows the entire square shape of the field arriving to the EPID, which is received in unattenuated parts (like in conventional linacs), attenuated parts, and missing parts. [Color figure can be viewed at wileyonlinelibrary.com]

2.B.2. IC array measurements

The array is used in two configurations. First, to measure dose at d_{max} (with 13 mm of buildup) at isocenter as a surrogate for dose measurements in the miniphantom for conventional linacs. Second, for measurements at 10 cm depth, the detector array is placed at 10 cm from surface of a 23-cm slab phantom, since the couch of the MR-linac does not allow for vertical motion and the isocenter lies at 13 cm above the couch.

2.B.3. Image processing

All acquired EPID images are preprocessed into the PV_{ij}^{proc}, which is the time-integrated pixel value EPID image corrected for the dark field, the flood field, and bad pixels,[5] and shifted 5.6 cm in the Y-direction to compensate for the off-axis alignment of the panel with respect to the beam.[38]

2.B.4. S_{ij} matrix

The S_{ij} matrix is a correction directly applied to each PV_{ij}^{proc} image to compensate for pixel sensitivity variations and off-axis differential photon energy.[41] Note that in MR-linac case, the S_{ij} matrix is also influenced by the attenuation of the beam through the MRI scanner between isocenter and EPID. The S_{ij} matrix is defined as follows:

$$S_{ij} = \frac{OCT_{ij}^{ISO \to EPID, 22x22}}{PV_{ij}^{proc, 22x22}} \quad (1)$$

where OCT is the measurement of a large field (22 × 22 cm^2) by the OCTAVIUS 1500 detector array at d_{max} positioned at isocenter and scaled to EPID level (using the ISQL). $PV_{ij}^{proc,22x22}$ is the corresponding EPID image after processing. The OCTAVIUS 2D array field was bilinearly interpolated, and later, a uniform smoothing over a 5 × 5 pixel neighborhood was performed to achieve the spatial resolution of the EPID.

2.B.5. Determination of the portal dose

Ideally, the conversion from pixel values to dose should be linear. The dose response D_r is defined as the ratio between the central region pixels and their corresponding dose measurement. The resulting image is called dose image:

$$D_{ij}^{EPID} = PV_{ij}^{proc} \cdot S_{ij} \cdot Dr \quad (2)$$

Note that the S_{ij} matrix was obtained with measurements performed with a large field (22 × 22 cm^2), so the dose image corresponds to the measured portal dose distribution only for this field size. However, the component of scatter from the MRI scanner toward the EPID, $Sc_{ij}^{MRI \to EPID}$, and the component of lateral scatter within the EPID, Sc_{ij}^{EPID}, are field size dependent. Hence, for any arbitrary field size, the dose image can be expressed as:

$$D_{ij}^{EPID} = PD_{ij}^{EPID'} + Sc_{ij}^{MRI \to EPID} + Sc_{ij}^{EPID}, \quad (3)$$

where $PD_{ij}^{EPID'}$ is the portal dose distribution measured for an arbitrary field size, without the extra effects of the cryostat, couch, and bridge, and the scatter of the EPID. The scatter from the MRI toward the EPID is modeled as a convolution between the dose image D_{ij}^{EPID} and a scatter kernel $K_{ij}^{MRI \to EPID}$. Simultaneously, the scatter occurring within the EPID Sc_{ij}^{EPID} is modeled as a deconvolution between the resulting dose image D_{ij}^{EPID} minus the scatter from the MRI to the EPID, and a scatter kernel K_{ij}^{EPID}:

$$Sc_{ij}^{MRI \to EPID} = D_{ij}^{EPID} \otimes K_{ij}^{MRI} \quad (4)$$

$$Sc_{ij}^{EPID} = (D_{ij}^{EPID} - Sc_{ij}^{MRI \to EPID}) \otimes^{-1} K_{ij}^{EPID} \quad (5)$$

As kernels, we use a Gaussian filter for $K_{ij}^{MRI \to EPID}$ and the kernel suggested in Ref. [[40] for the K_{ij}^{EPID}:

$$K_{ij}^{MRI} = \frac{c_{MRI}}{2\pi\sigma_{MRI}^2} exp\left(-\frac{r_{ij}^2}{2\sigma_{MRI}^2}\right) \quad (6)$$

$$K_{ij}^{EPID} = c_{DR}\begin{cases} c_1 \cdot \frac{e^{-\mu \cdot r_{ij}}}{r_{ij}^2} & \text{for} r_{ij} \neq 0 \\ 1 & \text{for} r_{ij} = 0 \end{cases}, \quad (7)$$

where r_{ij} is the distance of a pixel ij from the central axis and c_{MRI}, σ_{MRI}^2, c_{DR}, c_1, and μ are the kernel parameters. The portal dose in Eq. (3) is then calculated as:

$$PD_{ij}^{EPID'} = D_{ij}^{EPID} - \left(D_{ij}^{EPID} \otimes K_{ij}^{MRI \to EPID}\right) - \left(D_{ij}^{EPID} - \left(D_{ij}^{EPID} \otimes K_{ij}^{MRI \to EPID}\right)\right) \otimes^{-1} K_{ij}^{EPID} \quad (8)$$

Which is a function of the dose response Dr, and the parameters that determine the kernels K_{ij}^{EPID} and K_{ij}^{MRI} as expressed by:

$$PD_{ij}^{EPID'}\left(Dr, \sigma_{MRI}^2, c_{MRI}, c_{DR}, c_{1,}\mu\right) \quad (9)$$

The values of these model parameters are determined by a parametric fit of on-axis EPID-reconstructed dose values and the corresponding array measurements, for a set of field sizes ($2 \times 2 - 22 \times 22$ cm^2). For an accurate description of the portal dose image over the entire field of view, a 2D fitting procedure is finally introduced to minimize the difference in profiles of $PD_{ij}^{EPID'}$ images and array measurements. The corrected dose image PD_{ij}^{EPID} is defined as the dose image, $PD_{ij}^{EPID'}$ convolved with a kernel, K_{ij}^{prof}:

$$PD_{ij}^{EPID} = PD_{ij}^{EPID'} \otimes K_{ij}^{prof} \quad (10)$$

K_{ij}^{prof} is defined as a Gaussian kernel:

$$K_{ij}^{prof} = \frac{c_{prof}}{2\pi\sigma_{prof}^2} \exp\left(-\frac{r_{ij}^2}{2\sigma_{prof}^2}\right), \quad (11)$$

In order to determine the optimal σ_{prof}^2 and c_{prof} parameters of, K_{ij}^{prof}, the Euclidian distance between EPID and normalized measured profiles was minimized for all field sizes.

2.B.6. Final steps

After the portal dose image is calculated, the next steps of the adapted back-projection algorithm are identical to the conventional model: the portal dose is used to calculate the primary transmission using portal images with and without the phantom (or patient) in the beam. The primary dose within the phantom, Pr, is weighted with the Scatter-to-Primary Ratio (SPR) determined under reference conditions, $SPRr_{ref}$, which accounts for the thickness dependence of the scatter. The SPR is parametrized as a function of the primary transmission, the thickness of the patient, and the depth of the reconstruction plane. Next, the result is convolved with the scatter kernel $Kmid_{ij}$, accounting for the field size dependence of the scatter in the reconstruction plane.

2.C. Full commissioning at gantries 0°, 90°, 180°

In our back-projection algorithm for conventional linacs, all gantry angles are equivalent in terms of EPID pixel conversion to dose. Hence, the parameters of the back-projection model are commissioned using measurements performed at gantry 0°, which are applied for all gantry angles. The only gantry angle-dependent factor in the model is the correction for the attenuation of the couch top at the exit side of the patient. This is accounted for by a 2D couch attenuation model.[42] In the MR-linac geometry, however, the attenuation of the cryostat, couch, and bridge (at the exit side of the phantom) varies considerably with gantry angle. Ideally, the commissioning of the back-projection model would be performed for each possible gantry angle. However, as a gantry-mounted detector setup is not feasible within a slab phantom in the MR-linac, the commissioning process can only be carried out when the detector is perpendicular to the radiation beam, that is for gantry angles of 0°, 90°, 180°, and 270°. Because of symmetry on the setup, gantry angle 270° was omitted from this study. The set of measurements required for the full commissioning of our model is summarized in Table I.

2.D. IMRT plans validation at gantries 0°, 90°, 180°

At the time of this study, we chose patient categories that were likely to be treated first on the MR-linac. Three plans (two prostate and one rectum) were used, with around 1000 MU each, consisting of 25 beams (nine, nine, and seven, respectively) ranging from 5 to 20 segments per beam, with a largest irradiated segment per plan of 48–280 cm^2 were irradiated to a 23-cm slab phantom at the three gantry angles (0°, 90°, and 180°). Additionally, the 2D detector array was used to measure dose distributions at the isocenter level at 10 cm depth. The EPID images were back-projected to the isocenter plane using the adapted back-projection algorithm commissioned at the corresponding gantry angle. 2D γ analysis (3% global, 2 mm at 10% isodose) was performed between the detector array and EPID-reconstructed dose distributions. The reference point was determined as the point with the lowest gradient within the points with dose value equal to or greater than 80% of the maximum in the measured dose.

2.E. Gantry angle correction

A method was introduced to adapt the commissioning model for use at arbitrary gantry angles. This approach assumes that the differences between the different gantry configurations affect the S_{ij} matrix and the dose response. The modification of the S_{ij} Matrix is given by:

$$Sij_{ij}^{CGA \to AGA} = Sij_{ij}^{CGA} \frac{PV_{ij}^{proc,22x22,CGA}}{PV_{ij}^{proc,22x22,AGA}} \frac{OCT_{ij}^{ISO \to EPID,22x22,AGA}}{OCT_{ij}^{ISO \to EPID,22x22,CGA}} \quad (12)$$

TABLE I. Set of absolute dose measurements needed for the electronic portal imaging device (EPID) back-projection model commissioning in the MR-linac geometry. Note that an EPID image needs to be acquired for each of these measurements.

Measurement	Comment	Equipment	Phantom (cm^3)	Field size (cm^2)
S_{ij} matrix	To measure the relative sensitivity over the entire EPID and the 2D transmission through the MRI scanner	OCTAVIUS 1500 array at d_{max}		22 × 22
Field size series	No phantom, varying field size	OCTAVIUS 1500 array at d_{max}		2 × 2 − 20 × 20
Phantom series	Constant phantom thickness, varying field size	OCTAVIUS 1500 array at isocenter in slab phantom	30 × 30 × 20	2 × 2 − 20 × 20
Thickness series	Constant field size, varying phantom thickness	OCTAVIUS 1500 array at isocenter in slab phantom	30 × 30 × 4 − 32	10 × 10
Gantry angle correction	Large field at every gantry angle	OCTAVIUS 1500 array at d_{max}		22 × 22

where Sij_{ij}^{CGA} is the Sij matrix obtained at a commissioned gantry angle (CGA, i.e, 0°, 90°, or 180°) and $PV_{ij}^{proc,22x22,\mathrm{CGA}}$ and $PV_{ij}^{proc,22x22,GAC}$ correspond to the preprocessed open images of a 22 × 22 cm^2 field at a CGA and at an arbitrary gantry angle (AGA), respectively. $OCT_{ij}^{ISO\rightarrow EPID,22x22,\mathrm{CGA}}$ and $OCT_{ij}^{ISO\rightarrow EPID,22x22,AGA}$ are the 2D array measurements at isocenter at d_{max} for a 22 × 22 cm^2 field, scaled to the EPID level, both at CGA and AGA, respectively. Note that this correction requires the acquisition of an EPID image and a 2D array measurement of a large field (e.g., 22 × 22 cm^2) for each clinically relevant gantry angle, as included in Table I. However, since in this study, the validation of the method could only be performed with the 2D array positioned perpendicular to the beam, only data for gantries 0°, 90°, and 180° were acquired.

A normalization factor is applied to account for the differences in transmission leading to different dose response. Therefore, the dose response *Dr* is modified to fit the central region of a back-projected EPID image of a 10 × 10 cm^2 field irradiated to a slab phantom and back-projected to the isocenter at 10 cm depth, $\left\langle D_{ij}^{mid,10\times10}\right\rangle_{Roi}^{\mathrm{CGA}}$, to the dose measured with the array, $\left\langle OCT_{ij}^{10\times10}\right\rangle_{Roi}^{\mathrm{AGA}}$.

$$N^{AGA}=\frac{\left\langle D_{ij}^{mid,10\times10}\right\rangle_{Roi}^{\mathrm{CGA}}}{\left\langle OCT_{ij}^{10\times10}\right\rangle_{Roi}^{AGA}} \tag{13}$$

The adapted dose response is defined as:

$$Dr^{\mathrm{CGA}\rightarrow AGA}=Dr^{\mathrm{CGA}}N^{AGA} \tag{14}$$

where Dr^{CGA} is the dose response of the commissioned gantry angle, and N^{AGA} is the normalization factor.

2.F. Validation of adaptation to arbitrary gantry angles

To validate this approach, a full commissioning of the cardinal gantry angles was performed first, and three models were created. For each of the three models, the gantry angle correction can be applied. EPID images of IMRT fields irradiated at gantry 90° were back-projected using the model commissioned at gantry 0°, EPID images irradiated at gantry 180° were back-projected using the model commissioned at gantry 90° and EPID images acquired at gantry 0° were back-projected using the model of gantry 180°. The back-projected 2D dose distributions of the 25 IMRT beams were compared to the original array measurements of gantry angles 90° and 180° and 0°, respectively.

3. RESULTS

3.A. Validation of the algorithm

The performance of $K_{ij}^{MRI\rightarrow EPID}$, K_{ij}^{EPID}, and K_{ij}^{prof}, which correct for the presence of scatter at the EPID level, can be seen in Fig. 2, where EPID measured output factors before and after fitting to the IC measurements at isocenter are shown. Figure 3 presents the normalized EPID X profiles before and after applying the scatter kernelsK_{ij}^{prof}, K_{ij}^{EPID}, and$K_{ij}^{MRI\rightarrow EPID}$, compared to the measured dose profile with the detector array at isocenter at d_{max}, after scaling to the EPID level.

3.B. IMRT beams at gantries 0°, 90°, and 180°

Twenty-five IMRT fields from three treatments (two prostate, one rectum) were verified for the three commissioned gantry angles. An arbitrary subset of γ maps of these fields comparing detector array and EPID-reconstructed dose distributions is shown in Fig. 4**.** Table II reports the average and standard deviation of three parameters: γ-mean, γ-pass rate, and dose difference at the reference point ($\Delta Dose_{RP}$).

A sample of X and Y profiles of both EPID and array measured dose distributions at gantries 0°, 90°, and 180° is presented in Fig. 5, where the reference point is also indicated for each image.

3.C. Gantry angle dependency validation

The same EPID images acquired for the 25 IMRT fields at three gantry angles were used to validate the gantry angle

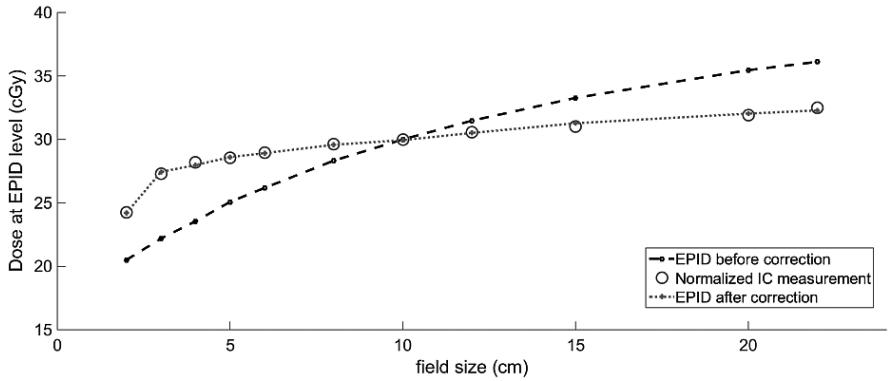

FIG. 2. Output factors measured with the 1500 OCTAVIUS detector array (open circles) and electronic portal imaging device (EPID) (lines). The normalized central pixel dose of the EPID before scatter correction is plotted in dashed black. After applying the scatter kernels K_{ij}^{EPID} and K_{ij}^{MRI}, the EPID signal corrected for the scatter is derived (dotted gray line). Note that for small fields (e.g., 2×2 cm^2), the measured dose on-axis might be underestimated due to possible small misalignments, the poor spatial resolution of the detector used in this study (1500 OCTAVIUS array), and the size of the ionization chambers.

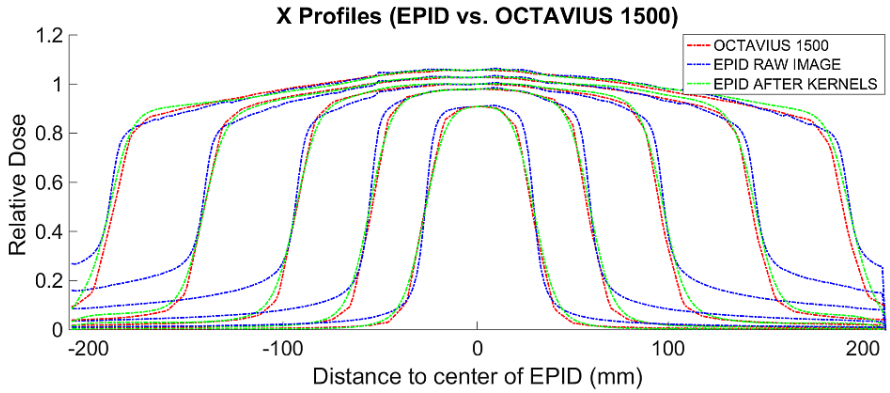

FIG. 3. X profiles of the raw (dashed blue) and after convolving with the scatter kernels (dashed green) EPID images for 3×3, 5×5, 10×10, 15×15, and 20×20 cm^2 square fields, compared to the profiles measured with the OCTAVIUS 1500 array (red). [Color figure can be viewed at wileyonlinelibrary.com]

correction method. The 25 images acquired at gantry angle 90° were back-projected using the model commissioned at gantry angle 0. Similarly, EPID images acquired at gantry angle 180° were back-projected using the model of gantry angle 90° and EPID images acquired at gantry angle 0° were back-projected using the model of gantry angle 180°. Dose difference at reference point and γ results are reported for the comparison to detector array measurements. Figure 6 shows the γ maps for the same fields as in Fig. 4, in this case using the gantry angle correction. Table III reports the averaged γ-mean and γ-pass rate together with the dose difference at a reference point (ΔDose_{RP}).

4. DISCUSSION

We successfully adapted our EPID dosimetry back-projection algorithm to the MR-linac geometry. Comparison of EPID-reconstructed and IC-measured 2D dose distributions at isocenter level shows good correspondence. This proof of concept study demonstrates that for three cardinal gantry angles, the algorithm is able to reconstruct the dose distribution inside a slab phantom accurately. Furthermore, a method is introduced to correct for the gantry angle-dependent attenuation of the cryostat, couch, and bridge, and was validated for gantry angles 0°, 90°, and 180°. Validation of this correction for arbitrary angles is beyond the scope of present work, as it involves IC array measurements that, with our current equipment, can only be performed at the cardinal angles. In future work, when expanding the method to all gantry angles, attenuation of the couch, bridge, and cryostat pipe will have to be taken into account in the back-projection algorithm. A method to correct for the influence of these structures will have to be developed and tested and the accuracy of such a method will have to be assessed.

The results presented in Table II suggest a minor underdosage in EPID-reconstructed dose. This can also be observed in some of the graphs in Fig. 5. To further determine whether this underdosage is systematic or not, more data would be required. An estimate of the uncertainty, obtained from the standard deviation of the reconstruction point doses of the 25 IMRT fields (Tables II and III), is 2% (1 SD).

The comparison between the EPID-reconstructed and IC array-measured dose distributions disregard any possible dose redistributions caused by the magnetic field inside the

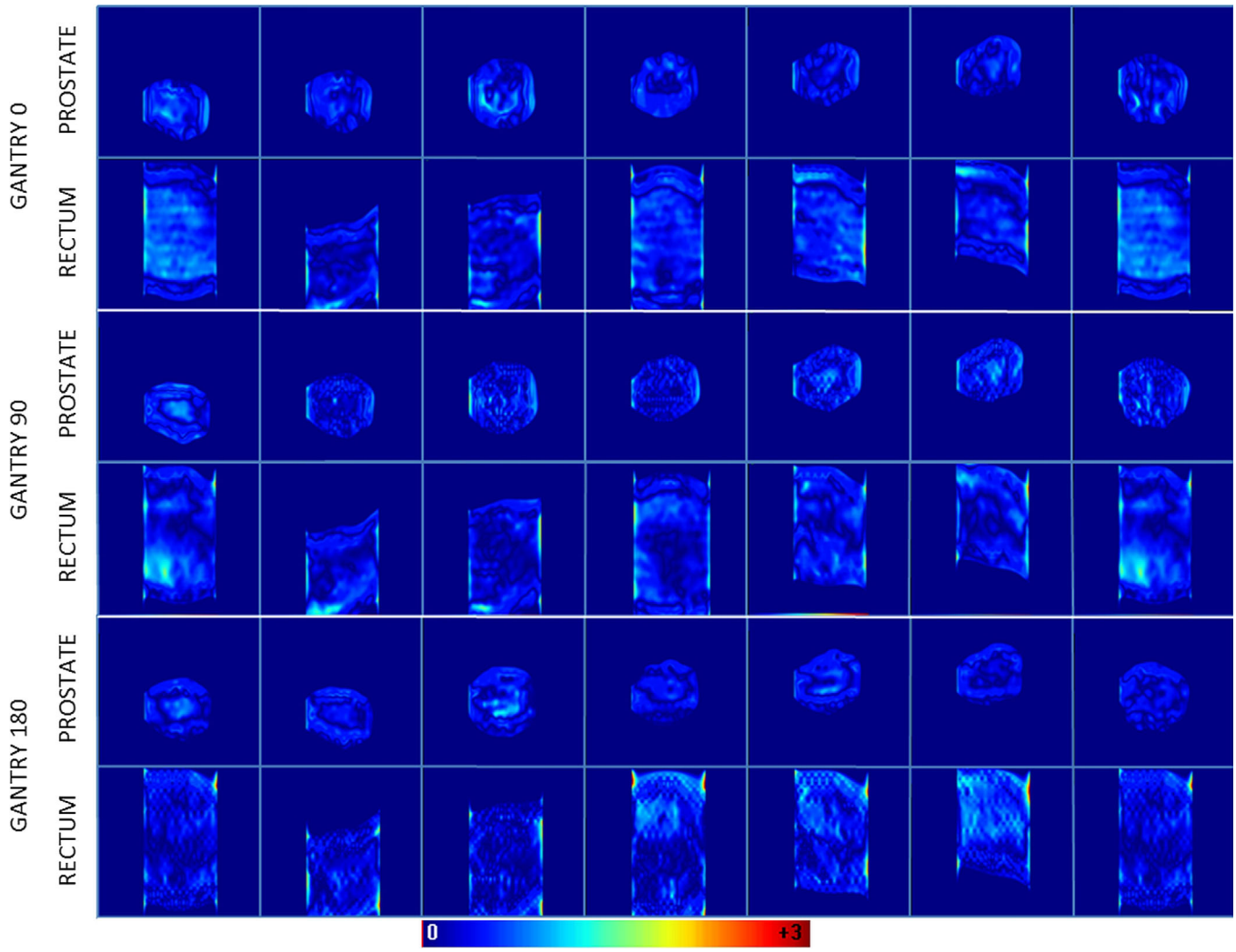

FIG. 4. The first two rows show a random subset of γ maps (3%, 2 mm, global 10% isodose) for seven prostate plans and seven rectum plans irradiated at gantry 0°. Rows 3 and 4 show the γ maps for the same rectum and prostate plans irradiated at 90°. The last two rows are the γ maps for the same fields irradiated at and 180°. [Color figure can be viewed at wileyonlinelibrary.com]

phantom due to the electron return effect (ERE). Our algorithm at this stage does not account for these effects. In this work, however, no inhomogeneities are present in the phantom geometry. Moreover, given the spatial resolution of the Octavius 2D array, we expect the impact of these effects to be negligible. Moreover, no skewness was observed in the S_{ij} matrix. Furthermore, the EPID measurements were fitted to array measurements performed in a 1.5 T B-field and the EPID-reconstructed dose was compared to dose distributions measured in a 1.5 T B-field, both showing good agreement.

In the patient geometry, however, the ERE might lead to important dose redistributions. So, it is expected that for EPID *in vivo* dosimetry, the current solution will fall short. EPID dosimetry can be a valuable tool for the detection of gross errors in the patient and for the detection of smaller deviations in situations where the effect of ERE is small. For instance, virtual in air EPID measurements[43] can be used to reconstruct EPID dose distributions to a phantom anatomy, instead of OCTAVIUS measurements which are more cumbersome by nature.

Several solutions can be thought of to solve this problem. First is the comparison of the EPID back-projected dose distribution to a copy of the planned dose distribution calculated without the magnetic field (i.e., a "nonmagnet" solution, similar to the "in-aqua" concept used for verification of lung treatments[44]). Alternatively, the back-projection algorithm could be modified to reconstruct the fluence in a plane before the patient and use it as input for a Monte Carlo dose calculation which accounts for the magnetic field, which can then be compared to the planned dose distribution. These approaches would, however, imply the use of a dose calculation engine, which would hamper fast computations in the verification process. The chosen technique to solve this problem is out of the scope of this work.

As with our conventional algorithm, the parameters of the model are determined using water-based kernels, and consequently, the model is expected to work most accurately for

TABLE II. Averaged γ results and dose difference at a reference point for 25 intensity-modulated radiation therapy fields at gantry 0°, 90°, and 180°.

Gantry angle	$\langle\gamma_{mean}\rangle$	$\langle$Passrate $\%_{\gamma<1}\rangle$	$\langle\Delta\text{Dose}_{RP}\rangle$
0	0.37 ± 0.07	97.9, 95% CI [96.7, 99.1]	−0.8% ± 1.8%
90	0.36 ± 0.09	98.1, 95% CI [97,5, 99,3]	−0.3% ± 1.9%
180	0.37 ± 0.06	97.9, 95% CI [97.2, 98.7]	−0.5% ± 1.7%

back-projection in homogeneous media (such as slab phantoms or the abdomen or pelvis. For dose verification in sites involving (large) tissue heterogeneities, for example, lung, esophagus, and breast, the same in aqua vivo approach as in the conventional algorithm can be used.[44] The performance of this approach will be assessed in future work.

Only pelvic treatments were included in this study. However, we expect the performance of the adapted back-projection algorithm to be treatment site independent.[45] Validation of the method in clinical practice falls outside the scope of this study.

Another limitation when using the EPID for dosimetry in the MR-linac in the current setup is that parts of beams exceeding 8.1 cm in the cranial direction cannot be detected due to the noncentered position of the panel. As a result, for treatments with large fields, parts of the reconstructed dose distribution will be missing, and cannot be verified. Due to the design of the MR-linac, alignment of the panel with the beam is not straightforward.

The extra attenuation of the beam by the cryostat outside the window ±5.6 cm in the longitudinal direction is another limitation of the MR-linac geometry and was not dealt with in current work. However, we are positive that the available signal in these strongly attenuated areas can be used for dosimetry purposes, although the accuracy of the final reconstructed dose distribution inside the phantom or patient will probably be lower. Overall, we observed that the verification of the treatments will be constrained by the size of the irradiated beams, and therefore, the accumulated EPID-reconstructed dose distribution may not be possible for certain target volumes. In clinical practice, this limitation does not

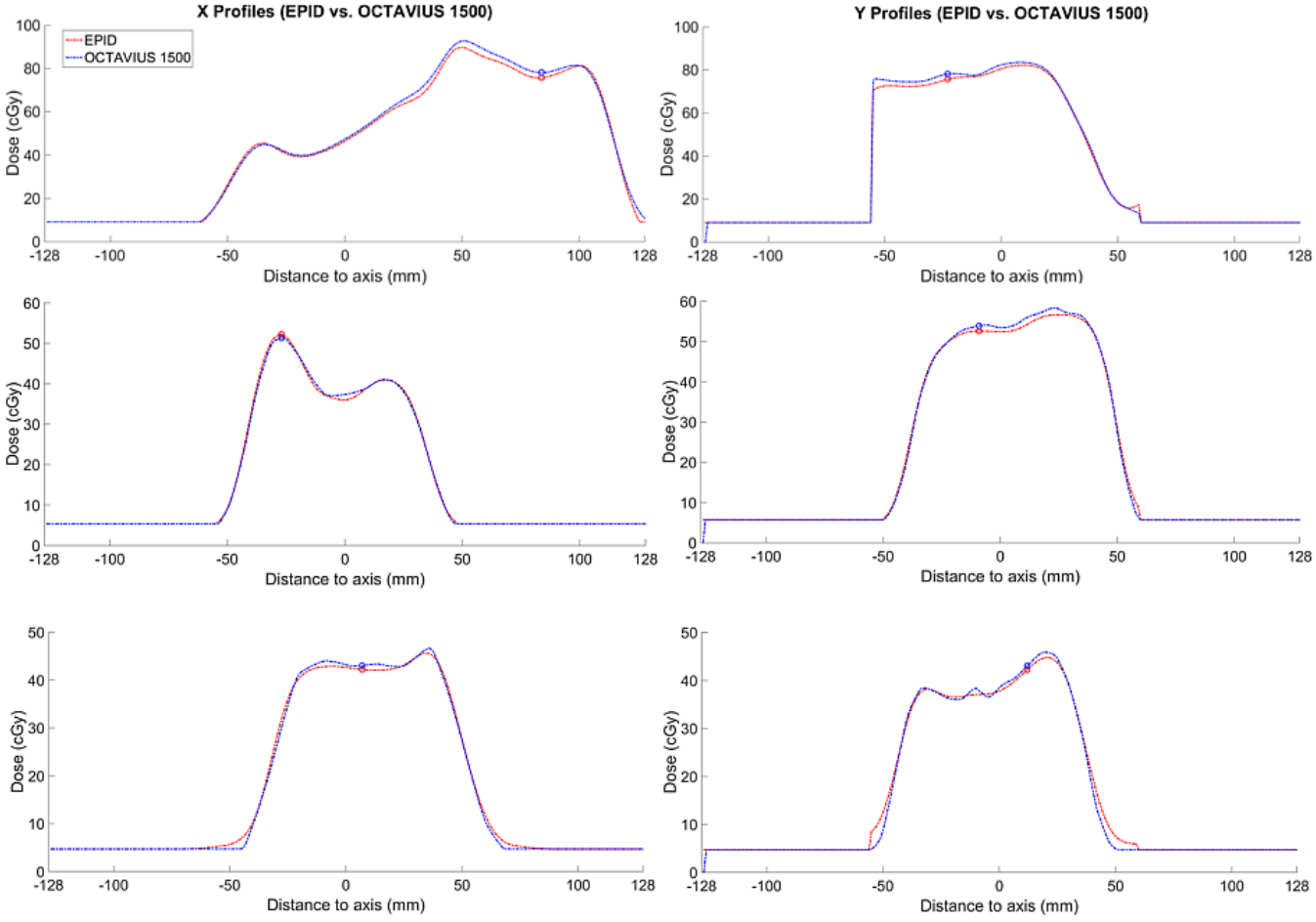

FIG. 5. X (left) and Y (right) electronic portal imaging device (EPID) and measured array profiles for one prostate intensity-modulated radiation therapy field (first row) and two rectum (second and third rows) IMRT fields irradiated at gantry angles 0° (first row), 90° (second row), and 180° (third row). EPID profiles are plotted in dashed red and array profiles in dashed blue. The blue and red circles determine the reference point where the dose difference was calculated. Note that, in the Y profile of the prostate beam, the signal of both EPID and array measured dose distributions were truncated at ±5.6 cm. [Color figure can be viewed at wileyonlinelibrary.com]

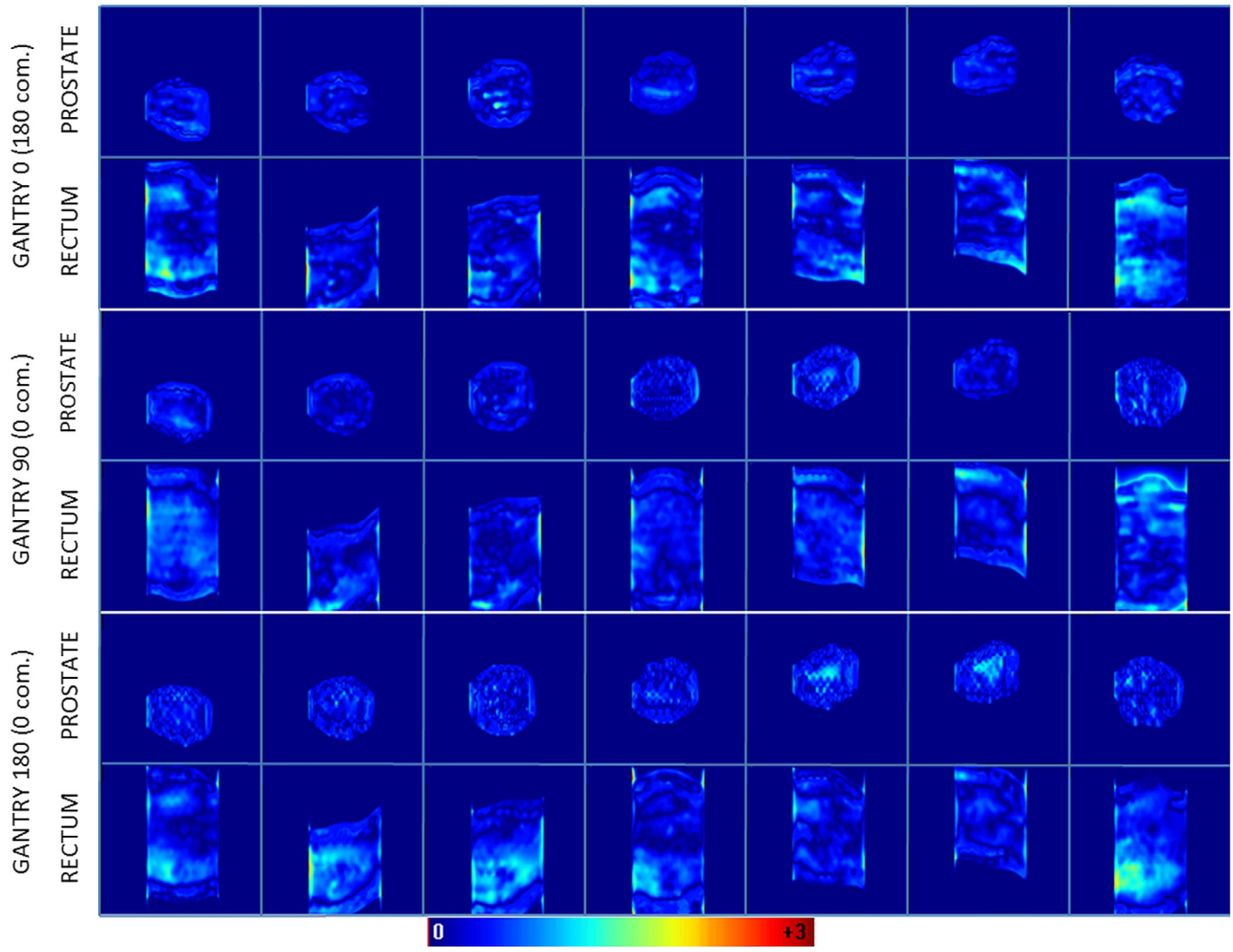

FIG. 6. The first two rows show a subset of γ maps (3%, 2 mm, global 10% isodose) for seven prostate plans and seven rectum plans irradiated at gantry 0° and reconstructed using the gantry angle correction from 180 → 0. Rows 3 and 4 show the γ maps for the same rectum and prostate plans irradiated at 90° and reconstructed using the correction 0 → 90. The last two rows are the γ maps for the same fields irradiated at 180° and reconstructed using the correction 90 → 180. [Color figure can be viewed at wileyonlinelibrary.com]

play a role for prostate and all stereotactic treatments. For treatments with field sizes exceeding the aforementioned window, we anticipate a hybrid approach with highest accuracy in the central region, and lower accuracy in the peripheral area.

In this proof of concept, EPID-based dose reconstruction at the isocenter plane is presented as a QA tool for the MR-linac in 2D. Future work includes the adaptation of this method to allow for 3D dose reconstructions for any gantry angle and comparison to planned dose distributions.

TABLE III. Average γ results and dose difference at a reference point for 25 intensity-modulated radiation therapy fields acquired at gantry 0°, 90°, and 180°, using the gantry adaptation solution and the models of gantries 180°, 0°, and 90° as a baseline, respectively.

Measurement/ model gantry angle	$\langle \gamma_{mean} \rangle$	$\langle$Passrate $\%_{\gamma<1}\rangle$	$\langle \Delta \text{Dose}_{RP} \rangle$
0°/180°	0.39 ± 0.07	97.9, 95% CI [97.7, 99.0]	−0.5% ± 2.1%
90°/0°	0.37 ± 0.08	98.4, 95% CI [97.3, 98.9]	−0.3% ± 1.8%
180°/90°	0.39 ± 0.07	97.9, 95% CI [96.5, 98.3]	0.5% ± 1.7%

5. CONCLUSIONS

Our EPID dosimetry back-projection algorithm was successfully adapted for the MR-linac geometry, accounting for the presence of the MRI housing between phantom (or patient) and EPID. Both the attenuation of the cryostat and the scatter from the cryostat reaching the panel were successfully modeled. The algorithm was commissioned at three gantry angles: 0°, 90°, and 180°. Excellent agreement was found for 25 IMRT beams between IC measured and EPID-reconstructed 2D dose distributions in a phantom positioned at the isocenter. Moreover, a solution is presented for the gantry angle dependence of the attenuation of cryostat, couch, and bridge. Validation of this method using data measured at a certain cardinal angle, but back-projected using the model

from another angle, again showed excellent agreement. This work is an essential step toward an accurate and independent integrated dose verification tool for the MR-linac.

ACKNOWLEDGMENTS

We thank Jochem Kaas, Thijs Perik, and Begoña Vivas for assistance with the measurements.

CONFLICTS OF INTEREST

Support for this research was provided, in part, by Elekta AB, Stockholm, Sweden.

[a]Author to whom correspondence should be addressed. Electronic mail: i.torres@nki.nl.

REFERENCES

1. McCurdy BM, Luchka K, Pistorius S. Dosimetric investigation and portal dose image prediction using an amorphous silicon electronic portal imaging device. *Med Phys*. 2001;28:911–924.
2. Greer PB, Popescu CC. Dosimetric properties of an amorphous silicon electronic portal imaging device for verification of dynamic intensity modulated radiation therapy. *Med Phys*. 2003;30:1618–1627.
3. Greer PB. Correction of pixel sensitivity variation and off-axis response for amorphous silicon EPID dosimetry. *Med Phys*. 2005;32(12):3558–3568.
4. Winkler P, Hefner A, Georg D. Dose-response characteristics of an amorphous silicon EPID. *Med Phys*. 2005;32:3095–3105.
5. Louwe RJW, McDermott LN, Sonke JJ, et al. The long-term stability of amorphous silicon flat panel imaging devices for dosimetry purposes. *Med Phys*. 2004;31:2989–2995.
6. McDermott LN, Louwe RJW, Sonke JJ, van Herk MB, Mijnheer BJ. Dose-response and ghosting effects of an amorphous silicon electronic portal imaging device. *Med Phys*. 2004;31:285–295.
7. Vial P, Gustafsson H, Oliver L, Baldock C, Greer PB. Direct-detection EPID dosimetry: investigation of a potential clinical configuration for IMRT verification. *Phys Med Biol*. 2009;54:7151–7169.
8. McCowan PM, McCurdy BMC. Frame average optimization of cine-mode EPID images used for routine clinical in vivo patient dose verification of VMAT deliveries. *Med Phys*. 2016;43:254–261.
9. Nijsten SMJJG, Mijnheer BJ, Dekker ALAJ, Lambin P, Minken AWH. Routine individualised patient dosimetry using electronic portal imaging devices. *Radiother Oncol*. 2007;83:65–75.
10. van Elmpt W, Nijsten S, Mijnheer B, Dekker A, Lambin P. The next step in patient-specific QA: 3D dose verification of conformal and intensity-modulated RT based on EPID dosimetry and Monte Carlo dose calculations. *Radiother Oncol*. 2008;86:86–92.
11. van Elmpt W, Nijsten S, Petit S, Mijnheer B, Lambin P, Dekker A. 3D in vivo dosimetry using megavoltage cone-beam CT and EPID dosimetry. *Int J Radiat Oncol Biol Phys*. 2009;73:1580–1587.
12. Wendling M, McDermott LN, Mans A, Sonke J-J, van Herk M, Mijnheer BJ. A simple backprojection algorithm for 3D in vivo EPID dosimetry of IMRT treatments. *Med Phys*. 2009;36:3310–3321.
13. Nelms BE, Rasmussen KH, Tomé WA. Evaluation of a fast method of EPID-based dosimetry for intensity-modulated radiation therapy. *J Appl Clin Med Phys*. 2011;11:140–157.
14. Berry SL, Polvorosa C, Cheng S, Deutsch I, Chao KSC, Wuu CS. Initial clinical experience performing patient treatment verification with an electronic portal imaging device transit dosimeter. *Int J Radiat Oncol Biol Phys*. 2014;88:204–209.
15. Francois P, Boissard P, Berger L, Mazal A. In vivo dose verification from back projection of a transit dose measurement on the central axis of photon beams. *Phys Med*. 2011;27:1–10.
16. Mans A, Remeijer P, Olaciregui-Ruiz I, et al. 3D Dosimetric verification of volumetric-modulated arc therapy by portal dosimetry. *Radiother Oncol*. 2010;94:181–187.
17. Van Uytven E, Van Beek T, McCowan PM, Chytyk-Praznik K, Greer PB, McCurdy BMC. Validation of a method for in vivo 3D dose reconstruction for IMRT and VMAT treatments using on-treatment EPID images and a model-based forward-calculation algorithm. *Med Phys*. 2015;42:6945–6954.
18. McCowan PM, Asuni G, Van Uytven E, et al. Clinical implementation of a model-based in vivo dose verification system for stereotactic body radiation therapy-volumetric modulated arc therapy treatments using the electronic portal imaging device. *Int J Radiat Oncol Biol Phys*. 2017;97:1077–1084.
19. Bedford JL, Hanson IM, Hansen VN. Portal dosimetry for VMAT using integrated images obtained during treatment. *Med Phys*. 2014;41:021725.
20. Persoon LCGG, Podesta M, Nijsten SMJJG, Troost EGC, Verhaegen F. Time-resolved versus integrated transit planar dosimetry for volumetric modulated arc therapy. *Technol Cancer Res Treatm*. 2016;15:NP79–NP87.
21. Raaijmakers AJE, Raaymakers BW, Lagendijk JJW, et al. Experimental verification of magnetic field dose effects for the MRI-accelerator.
22. Lagendijk JJW, Raaymakers BW, van Vulpen M. The magnetic resonance imaging-linac system. *Semin Radiat Oncol*. 2014;24:207–209.
23. Raaymakers BW, de Boer JCJ, Knox C, et al. Integrated megavoltage portal imaging with a 1.5 T MRI linac. *Phys Med Biol*. 2011;56:N207–N214.
24. Kupelian P, Sonke J. Magnetic resonance – guided adaptive radiotherapy: a solution to the future. *Semin Radiat Oncol*. 2014;24:227–232.
25. Houweling AC, De Vries JHW, Wolthaus J, et al. Performance of a cylindrical diode array for use in a 1.5 T MR-linac. *Phys Med Biol*. 2016;61:N80–N89.
26. Smit K, Kok JGM, Lagendijk JJW, Raaymakers BW. Performance of a multi-axis ionization chamber array in a 1.5 T magnetic field. *Phys Med Biol*. 2014;59:1845–1855.
27. De Vries JHW, Seravalli E, Houweling AC, et al. Characterization of a prototype MR-compatible Delta4 QA system in a 1.5 tesla MR-linac. *Phys Med Biol*. 2018;63:02NT02.
28. Lee HJ, Roed Y, Venkataraman S, Carroll M, Ibbott GS. Investigation of magnetic field effects on the dose–response of 3D dosimeters for magnetic resonance – image guided radiation therapy applications. *Radiother Oncol*. 2017;125:426–432.
29. Jochem K, et al. A fast automated sanity check for online plan adaptation in MR-guided RT. In: ESTRO37; 2018:P0-994.
30. Raaymakers BW, Jürgenliemk-Schulz IM, Bol GH, et al. First patients treated with a 1.5 T MRI-linac: clinical proof of concept of a high-precision, high-field MRI guided radiotherapy treatment. *Phys Med Biol*. 2017;62:L41–L50.
31. Vazquez-Quino LA, Huerta-Hernandez CI, Rangaraj D. Clinical experience with machine log file software for volumetric-modulated arc therapy techniques. *Baylor Univ Med Cent Proc*. 2017;30:276–279.
32. Chen G, Ahunbay E, Li XA. Technical Note : Development and performance of a software tool for quality assurance of online replanning with a conventional Linac or MR-Linac.
33. Kontaxis C, Bol GH, Stemkens B, et al. Towards fast online intrafraction replanning for free-breathing stereotactic body radiation therapy with the MR-linac. *Phys Med Biol*. 2017;62:7233–7248.
34. Glitzner M, Crijns SPM, de Senneville B, et al. On-line MR imaging for dose validation of abdominal radiotherapy. *Phys Med Biol*. 2015;60:8869–8883.
35. Neal B, Ahmed M, Kathuria K, et al. A clinically observed discrepancy between image-based and log-based MLC positions. *Med Phys*. 2016;43:2933.
36. Spreeuw H, Rozendaal R, Olaciregui-Ruiz I, et al. Online 3D EPID-based dose verification: Proof of concept. *Med Phys*. 2016;43:3969–3974.
37. Woodruff HC, Fuangrod T, Van Uytven E, et al. First experience with real-time epid-based delivery verification during IMRT and VMAT sessions. *Radiat Oncol Biol*. 2015;93:516–522.
38. Torres-Xirau I, Olaciregui-Ruiz I, Baldvinsson G, Mijnheer BJ, Van Der Heide UA, Mans A. Characterization of the a-Si EPID in the unity MR-linac for dosimetric applications. *Phys Med Biol*. 2018;63:025006.

39. Torres-Xirau I, Olaciregui-Ruiz I, Rozendaal R, et al. A back-projection algorithm in the presence of an extra attenuating medium : towards EPID dosimetry for the MR-Linac. *Phys Med Biol*. 2017;62:6322–6340.
40. Wendling M, Louwe RJW, McDermott LN, Sonke J-J, van Herk M, Mijnheer BJ. Accurate two-dimensional IMRT verification using a back-projection EPID dosimetry method. *Med Phys*. 2006;33:259–273.
41. Essers M, Hoogervorst BR, van Herk M, Lanson H, Mijnheer BJ. Dosimetric characteristics of a liquid-filled electronic portal imaging device. *Int J Radiat Oncol Biol Phys*. 1995;33:1265–1272.
42. Olaciregui-Ruiz I, Rozendaal R, Mijnheer B, Mans A. A 2D couch attenuation model for in vivo EPID transit dosimetry. *Biomed Phys Eng Expr*. 2017;4:5027.
43. Olaciregui-Ruiz I, Rozendaal R, van Oers RFM, Mijnheer B, Mans A. Virtual patient 3D dose reconstruction using in air EPID measurements and a back-projection algorithm for IMRT and VMAT treatments. *Phys Med*. 2017;37:49–57.
44. Wendling M, McDermott LN, Mans A, et al. In aqua vivo EPID dosimetry. *Med Phys*. 2011;39:367–377.
45. Mijnheer BJ, González P, Olaciregui-Ruiz I, Rozendaal RA, van Herk M, Mans A. Overview of 3-year experience with large-scale electronic portal imaging device-based 3-dimensional transit dosimetry. *Pract Radiat Oncol*. 2015;5:e679–e687.